

# Temperature and Metallicity in the Intra-cluster Medium of ABELL 262 observed with Suzaku

Kosuke SATO,<sup>1,2</sup> Kyoko MATSUSHITA,<sup>1</sup> and Fabio GASTALDELLO,<sup>3,4,5</sup>

<sup>1</sup> *Department of Physics, Tokyo University of Science, 1-3 Kagurazaka, Shinjuku-ku, Tokyo 162-8601*

<sup>2</sup> *Graduate School of Natural Science and Technology, Kanazawa University, Kakuma, Kanazawa, Ishikawa 920-1192*  
*ksato@astro.s.kanazawa-u.ac.jp*

<sup>3</sup> *IASF-Milano, INAF, via Bassini 15, Milano 20133, Italy*

<sup>4</sup> *Occhialini Fellow*

<sup>5</sup> *Department of Physics and Astronomy, University of California at Irvine, 4129 Frederick Reines Hall, Irvine, CA 92697-4575*

(Received 2008 August 1; accepted 2008 October 21)

## Abstract

We studied the temperature and abundance distributions of intra-cluster medium (ICM) in the Abell 262 cluster of galaxies observed with Suzaku. Abell 262 is a bright, nearby poor cluster with ICM temperature of  $\sim 2$  keV, thus providing useful information about the connection of ICM properties between groups and clusters of galaxies. The observed spectrum of the central region was well-represented by two temperature models, and the spectra for the outer regions were described by single temperature model. With the XIS instrument, we directly measured not only Si, S, and Fe lines but also O and Mg lines and obtained those abundances to an outer region of  $\sim 0.43 r_{180}$  for the first time. We found steep gradients for Mg, Si, S, and Fe abundances, while O showed almost flat abundance distribution. Abundance ratios of  $\alpha$ -elements to Fe were found to be similar to those of the other clusters and groups. We calculated the number ratio of type II to type Ia supernovae for the ICM enrichment to be  $3.0 \pm 0.6$  within  $0.1 r_{180}$ , and the value was consistent with those for other clusters and groups. We also calculated metal mass-to-light ratios (MLRs) for Fe, O and Mg (IMLR, OMLR, MMLR) with B-band and K-band luminosities of the member galaxies of Abell 262. The derived MLRs were comparable to those for other clusters with  $kT = 3\text{--}4$  keV.

**Key words:** galaxies: clusters: individual (Abell 262), galaxies: intergalactic medium, galaxies: abundances

## 1. Introduction

The metal abundances of Intra-cluster medium (ICM) carry a lot of information in understanding the chemical history and evolution of clusters. X-ray observations of ICM can immediately determine its temperature and metal abundances. Recent X-ray observations allow us to measure temperature and metal abundance distributions in the ICM based on the spatially resolved spectra. A large amount of metals of the ICM are mainly produced by supernovae (SNe) in early-type galaxies (Arnaud et al. 1992; Renzini et al. 1993), which are classified roughly as type Ia (SNe Ia) and type II (SNe II). In order to know how the ICM has been enriched, we need to measure the amount and distribution of metals in the ICM. Because Si and Fe are both synthesized in SNe Ia and II, we need to know O and Mg abundances, which are synthesized predominantly in SNe II, in resolving the past metal enrichment process in ICM by supernovae.

ASCA firstly showed the distribution of the heavy elements, such as Si and Fe, in the ICM (Fukazawa et al. 1998; Fukazawa et al. 2000; Finoguenov et al. 2000; Finoguenov et al. 2001), and BeppoSax also showed the Fe distribution and its gradient (De Grandi & Molendi

2001). Renzini (1997) and Makishima et al. (2001) summarized iron-mass-to-light ratios (IMLR) with B-band luminosity for various objects, as a function of their plasma temperature serving as a measure of the system richness, and IMLRs in groups were found to be smaller than those in clusters. They also showed that the early-type galaxies released large amount of metals which were probably formed through past supernovae explosions as shown earlier by Arnaud et al. (1992). In order to obtain a correct modeling of ICM, we need to know the correct temperature and metal abundance profiles without biases (e.g., Buote 2000; Sanders & Fabian 2002). Especially for the ICM of cooler systems, such as elliptical galaxies and groups of galaxies, sensitive observations are required as mentioned in Arimoto et al. (1997) and Matsushita et al. (2000).

Recent XMM-Newton and Chandra observations have enabled us to study the temperature structure, and detailed properties of the heavy elements in the ICM were shown based on the high spatial resolutions and small point spread functions (Fabian et al. 2001; Fabian et al. 2005; Fabian et al. 2006; Finoguenov et al. 2002; Xu et al. 2002; Gastaldello & Molendi 2002; Matsushita et al. 2003; Matsushita et al. 2007b; Tamura et al. 2003; Sanders

& Fabian 2007; Humphrey & Buote 2006; Rasmussen & Ponman 2007). In addition, the spatial distribution and elemental abundance pattern of the ICM metals were determined with the large effective area of XMM-Newton (Matsushita et al. 2007b; Tamura et al. 2004; Böhringer et al. 2005; O’Sullivan et al. 2005; Sanders & Fabian 2006; de Plaa et al. 2006; de Plaa et al. 2007; Werner et al. 2006; Simionescu et al. 2008). However, the abundance measurements of O and Mg with XMM-Newton, in particular for the outer regions of clusters, are quite difficult due to the relatively high intrinsic background. Suzaku XIS can measure all the main elements from O to Fe, because it realizes lower background level and higher spectral sensitivity, especially below 1 keV (Koyama et al. 2007). Suzaku observations have shown the abundance profiles of O, Mg, Si, S, and Fe to the outer regions with good precision for several clusters (Matsushita et al. 2007a; Sato et al. 2007a; Sato et al. 2008a; Sato et al. 2008b; Tokoi et al. 2008). Comparing the Suzaku results with supernova nucleosynthesis models, Sato et al. (2007b) showed the number ratios of SNe II to Ia to be 3.5.

Abell 262 (hereafter A 262) is a nearby cluster of galaxies ( $z = 0.0163$ ) characterized by a smooth and symmetric distribution of ICM, and is a richness class 0 cluster. A 262 is located on a knot of the large-scale filament of the Pisces-Perseus supercluster. A 262 is a very useful system in studying the history of chemical evolution of groups and clusters, because the ICM temperature is about  $\sim 2$  keV which is intermediate between clusters and groups of galaxies. The central cD galaxy, NGC 708, is a host of a double-lobed radio source, B20149+35 (Parma et al. 1986; Fanti et al. 1986). In the past, Einstein (David et al. 1993), ROSAT (David et al. 1996; Peres et al. 1998; Neill et al. 2001), ASCA (White 2000; Fukazawa et al. 2004), XMM-Newton (Peterson et al. 2003), and Chandra (Blanton et al. 2004) observed A 262, and ASCA showed an average temperature of  $kT = 2.13$  keV and an average metal abundance of 0.44 solar, respectively (Fukazawa et al. 2004). In a future paper (Gastaldello et al. 2008) we will investigate the mass and entropy radial profiles.

This paper reports on results from Suzaku observations of A 262 out to  $27' \simeq 540 h_{70}^{-1}$  kpc, corresponding to  $\sim 0.43 r_{180}$ . We use  $H_0 = 70$  km s $^{-1}$  Mpc $^{-1}$ ,  $\Omega_\Lambda = 1 - \Omega_M = 0.73$  in this paper. At a redshift of  $z = 0.0163$ ,  $1'$  corresponds to 19.9 kpc, and the virial radius,  $r_{180} = 1.95 h_{100}^{-1} \sqrt{k\langle T \rangle / 10 \text{ keV}}$  Mpc (Markevitch et al. 1998), is 1.25 Mpc ( $63'$ ) for an average temperature of  $k\langle T \rangle = 2.0$  keV. Throughout this paper we adopt the Galactic hydrogen column density of  $N_H = 5.38 \times 10^{20}$  cm $^{-2}$  (Dickey & Lockman 1990) in the direction of A 262. Unless noted otherwise, the solar abundance table is given by Anders & Grevesse (1989), and the errors are in the 90% confidence region for a single interesting parameter.

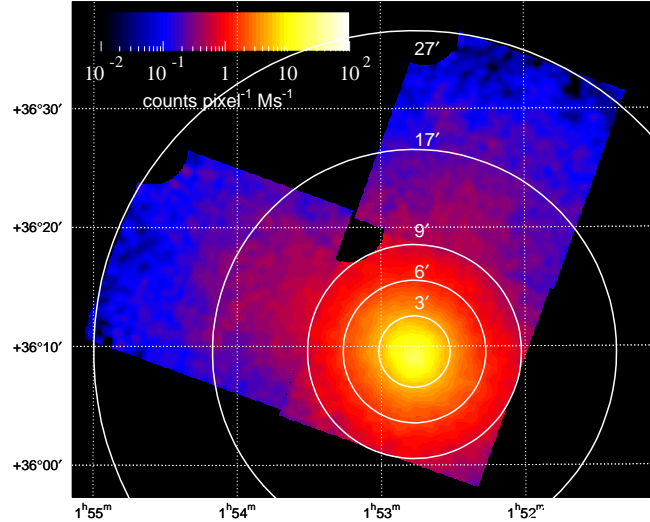


**Fig. 1.** Combined XIS image of central observation in the 0.5–4.0 keV energy range. The observed XIS0, 1, and 3 images were added on the sky coordinate after removing each calibration source region, and smoothed with  $\sigma = 16$  pixel  $\simeq 17''$  Gaussian. Estimated components of extragalactic X-ray background (CXB) and instrumental background (NXB) were subtracted, and the exposure was corrected, though vignetting was not corrected. The white circles show the extracted regions in the spectral fits.

## 2. Observations and Data Reduction

### 2.1. Observation

Suzaku observed the central and offset regions of Abell 262 in August 2007 (PI: F. Gastaldello and K. Matsushita). The observation log is given in table 1, and the XIS image in 0.5–4 keV is shown in figure 1. We analyzed only the XIS data in this paper, although Suzaku observed the object with both XIS and HXD. The XIS instrument consists of three sets of X-ray CCDs (XIS 0, 1, and 3). XIS 1 is a back-illuminated (BI) sensor, while XIS 0 and 3 are front-illuminated (FI). The instrument was operated in the Normal clocking mode (8 s exposure per frame), with the standard  $5 \times 5$  or  $3 \times 3$  editing mode.

### 2.2. Data Reduction

We used version 2.0 processing data, and the analysis was performed with HEASoft version 6.4.1 and XSPEC 11.3.2aj. Details of the analysis method are given in Sato et al. (2007a). Here we give just a brief description of the data reduction. The light curve of each sensor in the 0.3–10 keV range with a 16 s time bin was also examined in order to exclude periods with anomalous event rates which were greater or less than  $\pm 3\sigma$  around the mean to remove the charge exchange contamination Fujimoto et al. (2007), while Suzaku data was little affected by the soft proton flare compared with XMM data. The exposure after the screening was essentially the same as that before screening in table 1, which indicated that the non X-ray background (NXB) was almost stable during the observation. Event screening with cut-off rigidity (COR) was not performed

**Table 1.** Suzaku Observation logs for Abell 262.

Region	Seq. No.	Obs. date	(RA, Dec)* J2000	Exp. ksec	After screening (BI/FI) ksec
center	802001010	2007-08-17T04:13:43	(01 <sup>h</sup> 52 <sup>m</sup> 46 <sup>s</sup> 1, +36°09′33″)	37.2	37.0/37.0
offset1	802079010	2007-08-06T21:27:38	(01 <sup>h</sup> 54 <sup>m</sup> 08 <sup>s</sup> 3, +36°16′07″)	54.6	54.3/54.3
offset2	802080010	2007-08-08T01:52:10	(01 <sup>h</sup> 52 <sup>m</sup> 14 <sup>s</sup> 4, +36°26′08″)	54.7	54.3/54.4

\* Average pointing direction of the XIS, written in the RA\_NOM and DEC\_NOM keywords of the event FITS files.

in our data. In order to subtract the NXB and the extragalactic cosmic X-ray background (CXB), we employed the dark Earth database by the “xisnxbgen” Ftools task, and employed the CXB spectrum given by Kushino et al. (2002).

We generated two Ancillary Response Files (ARFs) for the spectrum of each annular sky region,  $A^U$  and  $A^B$ , which respectively assumed uniform sky emission and  $\sim 1^\circ \times 1^\circ$  size of the  $\beta$ -model surface brightness profile,  $\beta = 0.38$  and  $r_c = 0.47$ , in Fukazawa et al. (2004), by the “xissimarfgen” ftools task (Ishisaki et al. 2007). We also included the effect of the contaminations on the optical blocking filter of the XISs in the ARFs. Since the energy resolution also slowly degraded after the launch, due to radiation damage, this effect was included in the Redistribution Matrix File (RMF) by the “xisrmfgen” Ftools task.

### 3. Temperature and Abundance Profiles

#### 3.1. Spectral Fit

We extracted spectra from five annular regions of 0′–3′, 3′–6′, and 6′–9′ for the central observation, and 9′–17′, 17′–27′ for the offset regions, centered on (RA, Dec) = (1<sup>h</sup>52<sup>m</sup>46<sup>s</sup>1, +36°09′33″). Table 2 lists the areas of the extracted regions (arcmin<sup>2</sup>), fractional coverage of the annulus (%), the SOURCE\_RATIO\_REG values (%; see caption for its definition) and the BI and FI counts for the observed spectra and the estimated NXB and CXB spectra. The fraction of the background,  $f_{\text{BGD}} \equiv (\text{NXB} + \text{CXB})/\text{OBS}$ , was less than  $\sim 50\%$  even at the outermost annulus, although the Galactic component is not considered here. Each annular spectrum is shown in figure 2. The ionized Mg, Si, S, Fe lines are clearly seen in each region. The O VII and O VIII lines were prominent in the outer rings, however, most of the O VII line was considered to come from the local Galactic emission, and we dealt with those in the same way as Sato et al. (2007a) and Sato et al. (2008a).

The spectra with BI and FI for all regions were fitted simultaneously in the energy range 0.4–7.1 keV. In the simultaneous fit, the common Galactic emission component was included for all regions, while the A 262 emission was independently adjusted in each region. We excluded the narrow energy band around the Si K-edge (1.825–1.840 keV) because its response was not modeled correctly. The energy range below 0.4 keV was also excluded because the C edge (0.284 keV) seen in the BI spectra could not be reproduced well in our data. The range above 7.1 keV was

also ignored because Ni line ( $\sim 7.5$  keV) in the background left a spurious feature after the NXB subtraction at large radii. In the simultaneous fits of BI and FI data, only the normalization parameter was allowed to take different values between them.

It is important to estimate the Galactic component precisely. The Galactic component gives significant contribution especially in the outer regions, as shown in figure 2. However, the ICM component is still dominant in almost all the energy range except for the O VII line. We assumed two temperature *apec* model (assuming 1 solar abundance with redshift  $z = 0$ ) for the Galactic component, and fitted the data with the following model formula:  $constant \times (apec_{\text{cool}} + apec_{\text{hot}} + \text{ICMcomponents})$ , where we fixed the temperature of *apec*<sub>cool</sub> to be 0.074 keV as given by in Lumb et al. (2002). As a result, the best-fit normalization of the cool (0.074 keV) component turned out to be 0. When we fix the two temperatures to be the value in Lumb et al. (2002), the resultant parameters of the fit did not change significantly. Thus, we concluded that the two temperature model of the Galactic emission (the cool component temperature was fixed to be 0.074 keV) was enough to fit the A 262 data since the intensity of the Local Hot bubble in the A 262 direction seemed weak as shown in McCammon et al. (2002). In addition, we also examined the following model formula:  $constant \times (apec_{\text{hot}} + phabs \times (apec_{\text{cool}} + \text{ICM component}))$ , however the  $\chi^2$  values with this model were only a little worse than that with the above model. With this latter model, the results for the ICM component did not change significantly. The resultant normalizations of the *apec* models in table 3 are scaled so that they give the surface brightness in unit solid angle of arcmin<sup>2</sup>, and are constrained to give the same surface brightness and the same temperature for the simultaneous fits of all annuli.

The ICM spectrum for the central region,  $r < 3'$ , was clearly better represented by two *vapec* models than one *vapec* model in the  $\chi^2$  test. On the other hand, the ICM spectra for the outer regions,  $r > 3'$ , were well-presented by single temperature model. Thus, we carried out the simultaneous fit with the following formula of the Galactic and ICM components:  $constant \times (apec_{\text{cool}} + apec_{\text{hot}} + phabs \times (vapec_{0 < r < 27'} + vapec_{0 < r < 3'}))$ . The fit results are shown in table 3. The abundances were linked in the following way, Mg=Al, S=Ar=Ca, Fe=Ni, which gave good constraint especially for the offset regions. The abundances were also linked between the two *vapec* components for  $r < 3'$  region. Results of the spectral fit for individual annuli are summarized in table 3 and figure 3, in which system-

**Table 2.** Area, coverage of whole annulus, SOURCE\_RATIO\_REG, and observed/estimated counts for each annular region.

Region*	Area <sup>†</sup> (arcmin <sup>2</sup> )	Coverage <sup>†</sup>	SOURCE_RATIO_REG <sup>‡</sup>	Energy (keV)	BI counts <sup>§</sup>				FI counts <sup>§</sup>				
					OBS	NXB	CXB	$f_{\text{BGD}}$	OBS	NXB	CXB	$f_{\text{BGD}}$	
Center													
0'–3'	28.7	100.0%	13.6%	0.4–7.1	39,224	316	338	1.7%	57,652	336	534	1.5%	
3'–6'	84.8	100.0%	11.7%	0.4–7.1	37,674	953	871	4.8%	52,596	970	1,371	4.5%	
6'–9'	133.4	94.3%	9.8%	0.4–7.1	24,725	1,551	1,138	10.9%	33,040	1,510	1,705	9.7%	
Offset1													
9'–17'	121.2	18.5%	3.9%	0.4–7.1	13,956	1,704	1,448	22.6%	18,576	1,922	2,463	23.6%	
17'–27'	161.8	11.7%	3.3%	0.4–7.1	11,585	2,718	2,314	43.4%	13,507	2,514	3,398	43.8%	
Offset2													
9'–17'	119.9	18.3%	4.6%	0.4–7.1	12,625	1,945	1,582	27.9%	15,062	1,896	2,268	27.6%	
17'–27'	162.6	11.8%	3.1%	0.4–7.1	9,884	2,667	2,244	49.8%	12,367	2,640	3,571	50.2%	

SOURCE\_RATIO\_REG represents the flux ratio in the assumed spatial distribution on the sky ( $\beta$ -model) inside the accumulation region to the entire model, and written in the header keyword of the calculated ARF response by “xissimarfgen”.

\* The inner three regions correspond to the central observation, and the outer two regions correspond to the offset observations.

<sup>†</sup> The average values among four sensors are presented.

<sup>‡</sup> SOURCE\_RATIO\_REG  $\equiv$  COVERAGE  $\times \int_{r_{\text{in}}}^{r_{\text{out}}} S(r) r dr / \int_0^{\infty} S(r) r dr$ , where  $S(r)$  represents the assumed radial profile of Abell 262, and we defined  $S(r)$  in  $1^\circ \times 1^\circ$  region on the sky.

<sup>§</sup> OBS denotes the observed counts including NXB and CXB in 0.4–7.1 keV. NXB and CXB are the estimated counts.

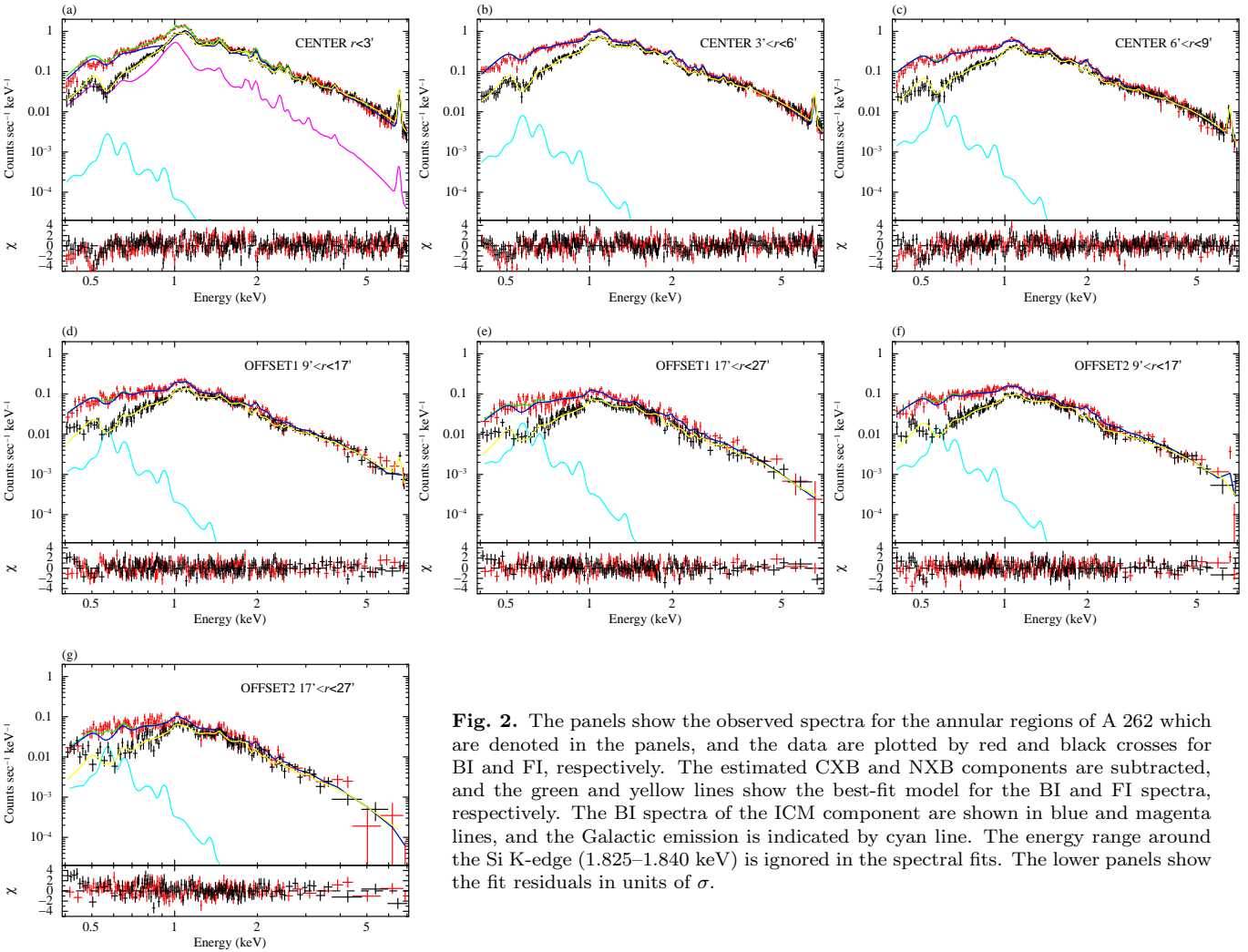


**Fig. 2.** The panels show the observed spectra for the annular regions of A 262 which are denoted in the panels, and the data are plotted by red and black crosses for BI and FI, respectively. The estimated CXB and NXB components are subtracted, and the green and yellow lines show the best-fit model for the BI and FI spectra, respectively. The BI spectra of the ICM component are shown in blue and magenta lines, and the Galactic emission is indicated by cyan line. The energy range around the Si K-edge (1.825–1.840 keV) is ignored in the spectral fits. The lower panels show the fit residuals in units of  $\sigma$ .

**Table 3.** Summary of the parameters of the fits to each annular spectrum of A 262. All annuli were simultaneously fitted. The values of Offset 1&2 correspond to the results of the summed spectra in the offset 1 and 2 regions. Errors are 90% confidence range of statistical errors, and do not include systematic errors. The solar abundance ratio of *angr* was assumed. These results are plotted in figure 3.

Galactic	$Norm_1^*$	$kT_1^\dagger$ (keV)	$Norm_2^*$	$kT_2$ (keV)		
	$0.00^{+2.25}_{-0.00}$	0.074(fix)	$0.96^{+0.54}_{-0.28}$	$0.174^{+0.036}_{-0.043}$		
ICM	$Norm_1^\ddagger$	$kT_1$ (keV)	$Norm_2^\ddagger$	$kT_2$ (keV)	$Norm_1/Norm_2$	$\chi^2/dof^\S$
Center						
0'-3'	$365.4^{+19.9}_{-20.7}$	$2.31^{+0.07}_{-0.06}$	$67.0^{+21.0}_{-22.3}$	$1.20^{+0.07}_{-0.10}$	$5.41^{+1.71}_{-1.81}$	895/497
3'-6'	$150.7^{+3.1}_{-2.8}$	$2.32^{+0.03}_{-0.03}$	—	—	—	726/498
6'-9'	$71.7^{+1.8}_{-1.7}$	$2.32^{+0.04}_{-0.04}$	—	—	—	648/498
Offset1						
9'-17'	$5.2^{+0.2}_{-0.2}$	$2.12^{+0.07}_{-0.06}$	—	—	—	364/382
17'-27'	$1.7^{+0.1}_{-0.1}$	$1.69^{+0.09}_{-0.04}$	—	—	—	399/382
Offset2						
9'-17'	$5.2^{+0.2}_{-0.2}$	$1.96^{+0.07}_{-0.07}$	—	—	—	408/382
17'-27'	$1.2^{+0.1}_{-0.1}$	$1.48^{+0.09}_{-0.07}$	—	—	—	530/379
total						3970/3018
Offset1&2						
9'-27'	$8.6^{+0.2}_{-0.2}$	$1.94^{+0.04}_{-0.04}$	—	—	—	4149/3044
ICM	O (solar)	Ne (solar)	Mg,Al (solar)	Si (solar)	S,Ar,Ca (solar)	Fe,Ni (solar)
Center						
0'-3'	$0.21^{+0.10}_{-0.10}$	$0.65^{+0.21}_{-0.20}$	$0.77^{+0.11}_{-0.10}$	$0.84^{+0.07}_{-0.07}$	$0.84^{+0.07}_{-0.07}$	$0.63^{+0.03}_{-0.03}$
3'-6'	$0.33^{+0.11}_{-0.12}$	$1.08^{+0.15}_{-0.15}$	$0.58^{+0.11}_{-0.11}$	$0.48^{+0.06}_{-0.06}$	$0.55^{+0.07}_{-0.07}$	$0.44^{+0.02}_{-0.02}$
6'-9'	$0.20^{+0.07}_{-0.13}$	$0.88^{+0.18}_{-0.17}$	$0.64^{+0.15}_{-0.15}$	$0.52^{+0.08}_{-0.08}$	$0.30^{+0.09}_{-0.09}$	$0.36^{+0.03}_{-0.03}$
Offset1						
9'-17'	$0.42^{+0.20}_{-0.20}$	$0.77^{+0.28}_{-0.26}$	$0.29^{+0.19}_{-0.18}$	$0.36^{+0.11}_{-0.11}$	$0.21^{+0.13}_{-0.14}$	$0.30^{+0.04}_{-0.04}$
17'-27'	$0.14^{+0.20}_{-0.14}$	$0.42^{+0.27}_{-0.14}$	$0.21^{+0.17}_{-0.17}$	$0.15^{+0.10}_{-0.10}$	$0.23^{+0.15}_{-0.15}$	$0.13^{+0.03}_{-0.03}$
Offset2						
9'-17'	$0.24^{+0.19}_{-0.19}$	$0.34^{+0.21}_{-0.20}$	$0.09^{+0.16}_{-0.09}$	$0.23^{+0.10}_{-0.10}$	$0.07^{+0.13}_{-0.07}$	$0.17^{+0.03}_{-0.03}$
17'-27'	$0.42^{+0.23}_{-0.25}$	$0.19^{+0.26}_{-0.19}$	$0.29^{+0.18}_{-0.17}$	$0.19^{+0.11}_{-0.10}$	$0.27^{+0.16}_{-0.16}$	$0.13^{+0.04}_{-0.03}$
Offset1&2						
9'-27'	$0.28^{+0.10}_{-0.10}$	$0.54^{+0.13}_{-0.12}$	$0.24^{+0.09}_{-0.09}$	$0.26^{+0.05}_{-0.05}$	$0.17^{+0.07}_{-0.07}$	$0.21^{+0.02}_{-0.02}$

\* Normalization of the *apec* component divided by the solid angle,  $\Omega^v$ , assumed in the uniform-sky ARF calculation (20' radius),  $Norm = \int n_e n_H dV / (4\pi(1+z)^2 D_A^2) / \Omega^v \times 10^{-20} \text{ cm}^{-5} \text{ arcmin}^{-2}$ , where  $D_A$  is the angular distance to the source.

† The value is shown in Lumb et al. (2002).

‡ Normalization of the *vapec* component scaled with a factor of SOURCE\_RATIO\_REG / AREA in table 2,  $Norm = \frac{\text{SOURCE\_RATIO\_REG}}{\text{AREA}} \int n_e n_H dV / [4\pi(1+z)^2 D_A^2] \times 10^{-20} \text{ cm}^{-5} \text{ arcmin}^{-2}$ , where  $D_A$  is the angular distance to the source.

§ All regions were fitted simultaneously.

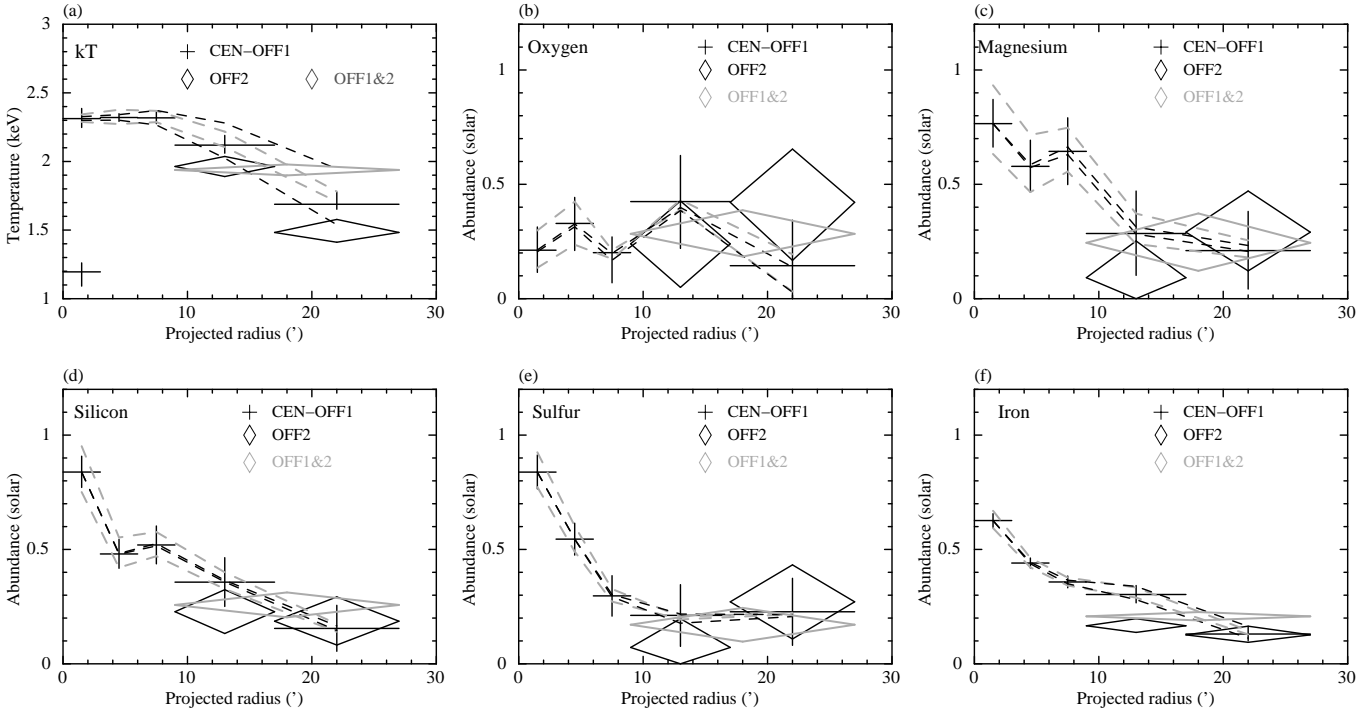


**Fig. 3.** (a): Radial temperature profiles derived from the spectral fits for each annulus against the projected radius. Light-gray diamonds correspond to the results of the addition of offset 1 and 2 spectra. Black dashed lines show systematic change of the best-fit values of the center–offset1 region by varying the thickness of the OBF contaminant by  $\pm 10\%$ . Light-gray dashed lines denote those when the estimated CXB and NXB levels are varied by  $\pm 10\%$ . (b)–(f): Radial abundance profiles are plotted in the same way as in (a).

atic error due to the OBF contamination and background (CXB + NXB) estimation are shown.

### 3.2. Temperature Profile

Radial temperature profile and the ratio of the *vapex* normalizations between the hot and cool ICM components are shown in figure 3(a) and table 3. The ICM temperature of hot and cool components at the central region was  $\sim 2.3$  and  $\sim 1.2$  keV, respectively, and the temperature decreased mildly to  $\sim 1.5$  keV in the outermost region. Our results for the two temperature ICM model are consistent with the Chandra result (Blanton et al. 2004) for the central region within  $3'$ . For the outer region ( $r > 3'$ ), our results are also consistent with the previous Chandra result (Vikhlinin et al. 2006), and the Chandra/XMM results (Gastaldello et al. 2007). The radius of  $27' \sim 540$  kpc corresponds to  $\sim 0.43 r_{180}$ , and the temperature decline, observed in several other clusters, is clearly recognized in this system out to this radius.

### 3.3. Abundance Profiles

Metal abundances are determined for the six element groups individually as shown in figures 3(b)–(f). The four abundance values for Mg, Si, S, and Fe and their radial variation look quite similar to each other. The central abundances lie around  $\sim 1.0$  solar, and they commonly decline to about  $1/5$  of the central value in the outermost annulus. Note that, although the Fe abundance decreased to  $r > \sim 20'$ ;  $0.3 r_{180}$ , the abundance at the outermost

region was determined with Fe-L line as shown in figure 2 because of the poor statistics around Fe-K line. On the other hand, the O profile looks flatter compared with the other elements. Because the results for the offset regions had large errors, we examined the summed spectra for these regions. However, even if the spectra in the  $9' < r < 17'$  and  $17' < 27'$  regions for both the offset1 and 2 observations were combined, the tendency of the radial abundance distributions did not change significantly. We also noted that, when we examined all abundances to be free in the fits, the resultant parameters did not change within the statistical errors.

### 3.4. Systematic Errors and Uncertainties

We performed the spectral fits with the *vmekal* model instead of the *vapex* model. As a result, the abundance profiles did not change within the statistical errors, although the Mg abundances with the *vmekal* model were  $\sim 30$ – $40\%$  lower than those with the *vapex* model.

We examined the systematic error of our results by changing the background normalization by  $\pm 10\%$ , and the error range is plotted with light-gray dashed lines in figure 3. The systematic error due to the background estimation is almost negligible. The other systematic error concerning the uncertainty in the OBF contaminant is shown by black dashed lines as shown in figure 3. A list of  $\chi^2/\text{dof}$  by changing the systematic errors is presented in table 4. Although the fit is not statistically acceptable due mainly to the very high photon statistics compared

**Table 4.** List of  $\chi^2/\text{dof}$  for the fits of the nominal and considering the systematic errors such as contaminant of OBF and background level. For details, see text.

Region	nominal	contaminant		background	
		+10%	-10%	+10%	-10%
All .....	3970/3018	3769/3018	4350/3018	4041/3018	3997/3018

with the systematic errors in the instrumental response, these results are useful to assess whether each element abundance is reasonably determined or not. We note that Ne abundance is not reliably determined due to an overlap with the strong and complex Fe-L line emissions, however we left these abundance to vary freely during the spectral fit.

Oxygen abundance is strongly affected by the Galactic emission as shown in Sato et al. (2007a). However, we have shown that the use of different temperature models for the Galactic emission did not significantly affect the abundance results as mentioned in subsection 3.1. We also examined radial surface brightness profiles of the O VII and O VIII emission lines in order to see if they are spatially uniform or peaked at the cluster center. The surface brightness of the lines was derived by fitting the annular spectrum with a *power-law + gaussian + gaussian* model for an energy range between 500 and 700 eV. In this fit, we fixed the Gaussian  $\sigma$  to be 0, and allowed the energy center of the two Gaussians to vary within 555–585 eV or 630–660 eV for O VII or O VIII line, respectively. The derived line intensities are shown in figure 4. There is a clear excess in the O VIII intensity profile towards the cluster center, while O VII one is consistent to be constant as already noticed by Sato et al. (2007a); Sato et al. (2008a); Sato et al. (2008b). This is a clear evidence that the O VIII line is associated with the ICM itself, on the other hand, O VII line may mainly come from the Galaxy or from the interplanetary space.

## 4. Discussion

### 4.1. Metallicity Distribution in the ICM

The present Suzaku observation of A 262 shows the abundance distribution of O, Mg, Si, S, and Fe out to a radius of  $27' \simeq 540$  kpc, which corresponds to  $\sim 0.43 r_{180}$ , as shown in figure 3. The Ne abundance shows a large ambiguity due to the strong coupling with Fe-L lines. Distributions of Mg, Si, S, and Fe are similar to each other, while O profile in the outer region shows a large uncertainty. We plotted abundance ratios of O, Mg, Si, and S over Fe as a function of the projected radius in figure 5. The ratios Mg/Fe, Si/Fe and S/Fe are consistent with a constant value around 1.5–2, while O/Fe ratio for the innermost region ( $r < 2'$ ) is lower around 0.5. In addition, the O/Fe ratio suggests some increase with radius. The Fe abundance at the outermost region has a large uncertainty compared with that in the inner regions, because the value in the outer region was determined by Fe-L line as shown in figure 2. We note that these abundance profiles are not deconvolved and averaged over the line of

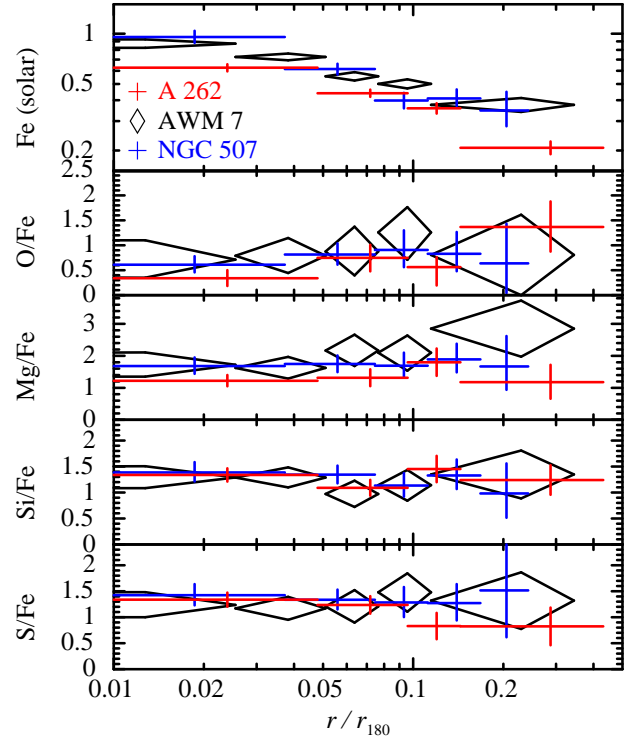


**Fig. 5.** Comparison of the abundance ratio for A 262 (red) with results for the AWM 7 cluster (black diamonds; Sato et al. 2008a) and NGC 507 group (blue crosses; Sato et al. 2008b). Fe abundance and the O/Fe, Mg/Fe, Si/Fe, and S/Fe abundance ratios in solar units (Anders & Grevesse 1989) are plotted against the projected radius scaled by the virial radius,  $r_{180}$ , in all panels.

sight.

Recent Suzaku observations have presented abundance profiles in several other systems: an elliptical galaxy NGC 720 (Tawara et al. 2008), a group of galaxies HCG 62 (Tokoi et al. 2008) and NGC 507 (Sato et al. 2008b), the Fornax cluster and NGC 1404 (Matsushita et al. 2007b), and a cluster of galaxies Abell 1060 (Sato et al. 2007a) and AWM 7 (Sato et al. 2008a). All systems show very similar value of Si/Fe ratio, to be 1–1.5. Mg/Fe ratio is slightly higher in HCG 62, Abell 1060 and AWM 7 than in other systems. We compare metal abundances of A 262 with those of AWM 7 and NGC 507 as shown in figure 5. Because AWM 7 ( $\sim 3.5$  keV) and NGC 507 ( $\sim 1.5$  keV) host cD galaxies at the center and are similar to A 262 in the X-ray morphology. A 262 may connect groups of galaxies and poor clusters regarding our understanding of the cluster evolution. Although the Fe abundance of A 262 is slightly lower than that of the AWM 7 and NGC 507 in the central region, the Fe profile to the outer region

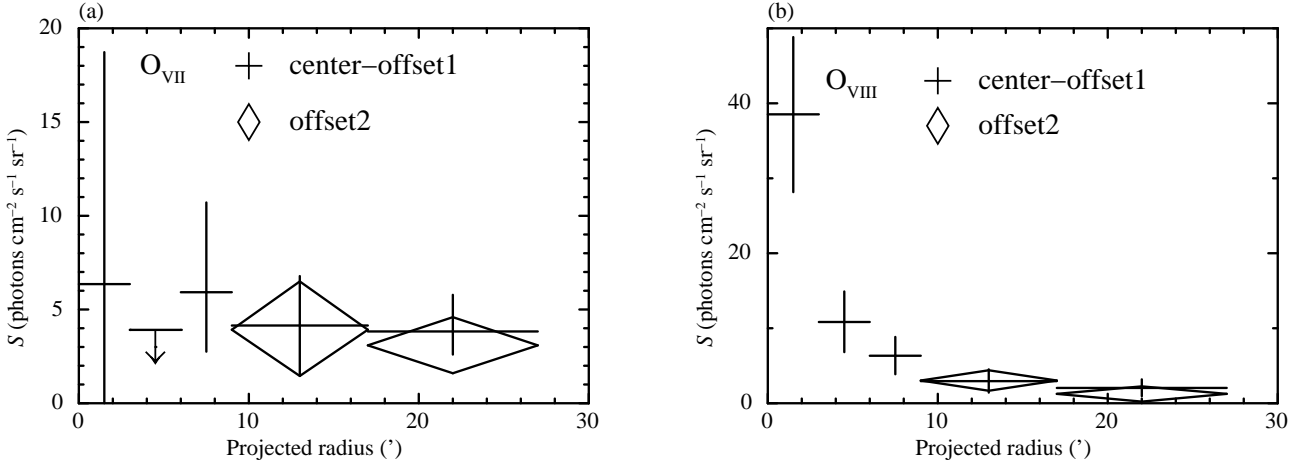


Fig. 4. Intensities of (a) O VII and (b) O VIII lines at each annulus of A 262 in units of photons  $\text{cm}^{-2} \text{s}^{-1} \text{sr}^{-1}$ .

looks quite similar. Abundance ratios of O/Fe, Mg/Fe, Si/Fe, and S/Fe are also quite similar between the three systems. Therefore, the abundance ratios show closer similarity than the absolute abundance values among different systems. The efficiency of the metal enrichment may depend on parameters such as age, star-formation efficiency, and contribution from cD galaxies. However, the relative contribution of SNe Ia and II and the process of metal mixing in the ICM seem to be quite similar among different clusters and groups.

Tamura et al. (2004) reported abundance ratios for 19 clusters studied with XMM-Newton, and the mean Si/Fe ratio in cool and medium temperature clusters with  $kT < 6$  keV was  $\sim 1.4$ . This is consistent with the Suzaku results for groups and poor clusters including A 262. Their O/Fe ratio,  $\sim 0.6$ , in the cluster core also agrees with the Suzaku results including our A 262 case. Matsushita et al. (2003) and Matsushita et al. (2007a) reported abundance ratios for M87 and the Centaurus cluster, respectively, based on XMM-Newton observations. M87 showed Mg/O ratio to be  $\sim 1.3$  in the central region, and the Centaurus cluster indicated O/Fe and Si/Fe ratios within  $8'$  to be  $\sim 0.5$  and  $\sim 1.0$ , respectively, and they were consistent with our results. Sanders & Fabian (2006) also showed the abundance ratios for the Centaurus cluster with Chandra and XMM-Newton, and the radial abundance ratios of O/Fe, Mg/Fe, and Si/Fe to be  $0.5 - 1.0$ ,  $\sim 1.0$ ,  $\sim 1.2$ , respectively, were consistent with our results.

#### 4.2. Number Ratio of SNe II to SNe Ia

In order to examine the SNe Ia and SNe II contribution to the ICM metals, the elemental abundance pattern of O, Mg, Si, S and Fe was examined for the region within  $0.1$  and  $0.27 r_{180}$ . The abundance ratios at  $r \sim 0.3 r_{180}$  and  $0.3 < r < 0.4 r_{180}$ , with the latter corresponding to the outermost region, look similar within the statistic errors. The relative abundance ratios to Fe were fitted by a combination of average SNe Ia and SNe II yields per supernova, as shown in figure 6. The fit parameters were chosen to be the integrated number of SNe Ia ( $N_{\text{Ia}}$ ) and the number

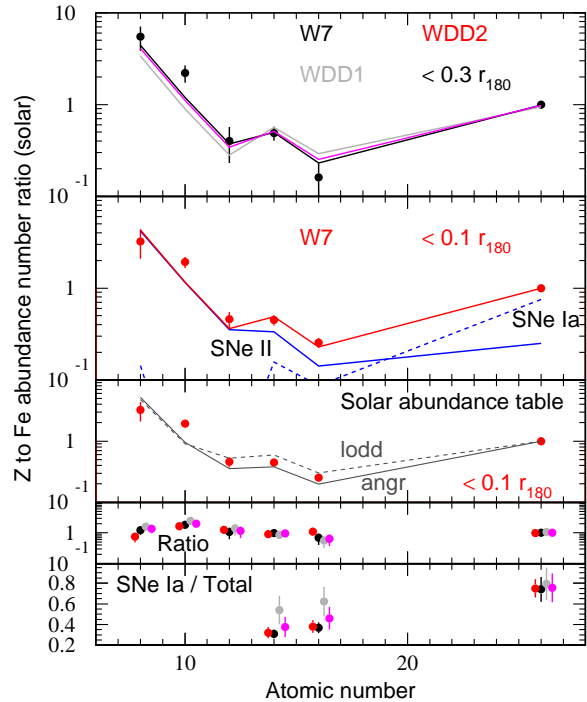


Fig. 6. Fit results of number ratios of elements to Fe of A 262. Top and second panel show the abundance number ratios in solar unit within  $0.27 r_{180}$  (black) and  $0.1 r_{180}$  (red) regions, respectively. Blue dashed and solid lines in the second panel correspond to the contributions of SNe Ia (W7) and SNe II within  $0.1 r_{180}$ , respectively. Ne (atomic number = 10) is excluded in the fit. Third panel shows the comparison with solar abundance table of Anders & Grevesse (1989) (light-gray line) and Lodders (2003) (dashed light-gray line). Fourth panel indicates ratios of data points to the best-fit model. Bottom panel indicates fractions of the SNe Ia contribution to total metals in the best-fit model for each element, respectively.

**Table 5.** Integrated number of SNe I ( $N_{\text{Ia}}$ ) and number ratio of SNe II to SNe Ia ( $N_{\text{II}}/N_{\text{Ia}}$ ).

Region	SNe Ia Model	$N_{\text{Ia}}$	$N_{\text{II}}/N_{\text{Ia}}$	$\chi^2/\text{dof}$
$< 0.1 r_{180}$	W7	$4.4 \pm 0.4 \times 10^8$	$3.0 \pm 0.6$	8.6/3
$< 0.27 r_{180}$	W7	$2.7 \pm 0.9 \times 10^9$	$3.2 \pm 1.0$	4.1/3
$< 0.1 r_{180}$	WDD1	$5.1 \pm 0.4 \times 10^8$	$1.8 \pm 0.5$	27.2/3
$< 0.27 r_{180}$	WDD1	$2.9 \pm 1.1 \times 10^9$	$2.1 \pm 0.9$	19.6/3
$< 0.1 r_{180}$	WDD2	$4.2 \pm 0.4 \times 10^8$	$2.9 \pm 0.6$	9.2/3
$< 0.27 r_{180}$	WDD2	$2.5 \pm 0.9 \times 10^9$	$3.1 \pm 1.0$	7.6/3

ratio of SNe II to SNe Ia ( $N_{\text{II}}/N_{\text{Ia}}$ ), because  $N_{\text{Ia}}$  could be well constrained by the relatively small errors in the Fe abundance. The SNe Ia and II yields were taken from Iwamoto et al. (1999) and Nomoto et al. (2006), respectively. We assumed a Salpeter IMF for stellar masses from 10 to 50  $M_{\odot}$  with the progenitor metallicity of  $Z = 0.02$  for SNe II, and W7, WDD1 or WDD2 models for SNe Ia. Table 5 and figure 6 summarizes the fit results. The number ratios were better represented by the W7 SNe Ia yield model than by WDD1. The number ratio of SNe II to SNe Ia with W7 is  $\sim 3.2$  within  $0.3 r_{180}$ , while the ratio with WDD1 is  $\sim 2.1$ . The WDD2 model gave the result quite similar to those of W7. The resultant number ratios are consistent with those in Sato et al. (2007a). We also compared the abundance pattern of A 262 with the solar abundance. The third panel in figure 6 shows the comparison of the abundance pattern within  $r < 0.1 r_{180}$  of A 262 with the solar abundance pattern in Anders & Grevesse (1989) and Lodders (2003). Our results of Mg, Si, and S fall between the abundance patterns of Anders & Grevesse (1989) and Lodders (2003).

Almost  $\sim 80\%$  of Fe and  $\sim 30\%$  of Si and S were synthesized by SNe Ia in the W7 model, as demonstrated in the bottom panel of figure 6. The observed tendency of  $\sim 2$  keV cluster is similar to those of  $\sim 3$  keV clusters in Sato et al. (2007a). The values in table 5 imply that the  $N_{\text{II}}/N_{\text{Ia}}$  ratio behaves in a similar manner for different supernova models between  $r < 0.1 r_{180}$  and  $r > 0.1 r_{180}$ . We note that the fit was not acceptable based on the  $\chi^2$  value in table 5. As described in Sato et al. (2007a), the models adapted here (SNe yeild, Salpeter IMF, etc.) are probably too simplified.

#### 4.3. Metal Mass-to-Light Ratio

Combining the abundance profile obtained with Suzaku and the 3-dimensional gas mass profile with Chandra and XMM-Newton (Gastaldello et al. 2007), we calculated cumulative metal mass as shown in figure 7(a). In order to see whether the gas mass profile derived from Chandra/XMM observations could apply to the offset regions of Suzaku which were out of the field of view of Chandra/XMM observations, we compared three surface brightness profiles: 1. the Chandra/XMM observations which were used to derive the mass profiles, 2. the ASCA observations which were used to calculate ARFs, and 3. the present Suzaku observation. However, we could not compare these three profiles directly because of the poor angular resolution and vignetting effect of Suzaku

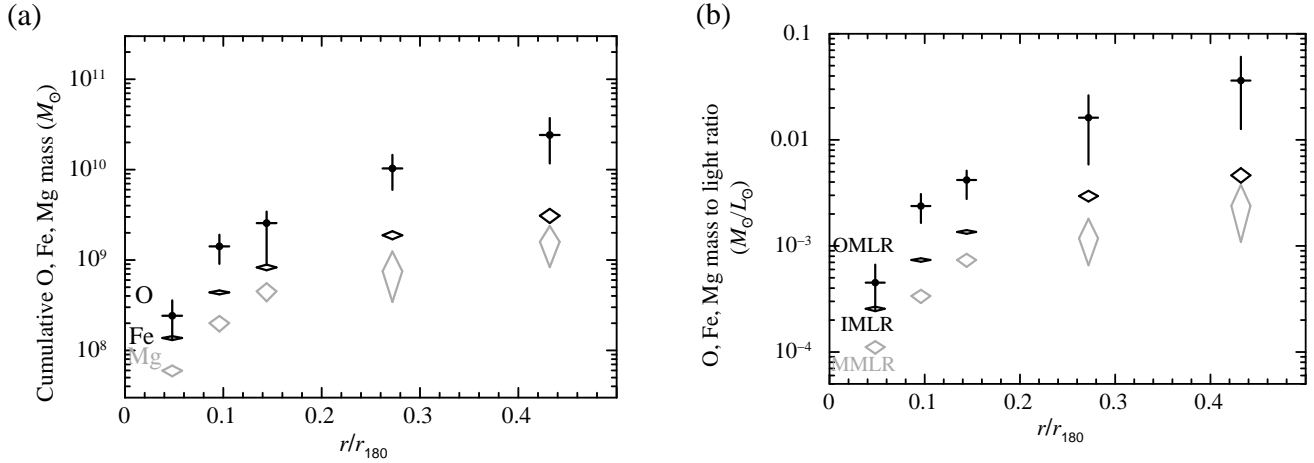
as shown in Sato et al. (2007a). Thus, we need to simulate the surface brightness profiles using the parameters of the XMM/Chandra and ASCA observations with “xis-sim” Ftools task. As a result, those profiles were consistent with that of this Suzaku observation within  $r < 13'$ , or 260 kpc. On the other hand, the profile in  $r > 20'$  looked slightly different, and the observed Suzaku profile was slightly steeper than those of Chandra/XMM and ASCA. Thus, the derived metal mass has a systematic error by about a factor of 2. The derived iron, oxygen, and magnesium mass within the 3-dimensional radius of  $r < 540$  kpc are  $3.1 \times 10^9$ ,  $2.4 \times 10^{10}$ , and  $1.6 \times 10^9 M_{\odot}$ , respectively. Errors of the metal mass plotted in figure 7(a) are taken from the statistical errors of each elemental abundance in the spectral fits, because the statistical errors of the fits are larger than those of the gas mass profiles in Gastaldello et al. (2007).

We examined metal mass-to-light ratios for oxygen, iron, and magnesium (OMLR, IMLR, and MMLR, respectively) to compare the ICM metal distribution with the stellar mass profile. Although, historically, B-band luminosity has been used for the estimation of the stellar mass (Makishima et al. 2001), we calculated the K-band luminosity in A 262 based on the Two Micron All Sky Survey <sup>1</sup> with the Galactic extinction,  $A_K = 0.032$ , from NASA/IPAC Extragalactic Database (NED) in the direction of A 262. We used  $2^{\circ} \times 2^{\circ}$  data set centered at the A 262 position as shown in table 1, and subtracted the  $r > 1^{\circ}$  region as the background. In addition, we deprojected the luminosity profile as a function of radius. The resultant luminosity within this Suzaku observation,  $r < 27'$ , is  $6.7 \times 10^{11} L_{\odot}$  in K-band. The radial luminosity profile is not directly plotted, but it can be inferred from the ratio of the metal mass in figure 7(a) divided by the metal mass to light ratio in (b). We calculated the integrated values of OMLR, IMLR, and MMLR with K-band within  $r \lesssim 540$  kpc as shown in figure 7(b) and table 6, and their values turned out to be  $\sim 3.6 \times 10^{-2}$ ,  $\sim 4.6 \times 10^{-3}$ , and  $\sim 2.4 \times 10^{-3} M_{\odot}/L_{\odot}$ , respectively. The errors are only based on the statistical errors of metal abundance in the spectral fit, and the uncertainties of the gas mass profile and the luminosity of member galaxies are not included. Note that the derived luminosity profiles were not corrected the Suzaku PSF effect, because the errors of MLRs were dominated by the error of the metal mass compared with that of the light luminosity.

<sup>1</sup> The database address: <http://www.ipac.caltech.edu/2mass/>

**Table 6.** Integrated mass-to-light ratios of O, Mg, and Fe (OMLR, MMLR, IMLR ) with K-band luminosity in units of  $M_{\odot}/L_{\odot}^K$ .

Region (kpc/ $r_{180}$ )	OMLR	MMLR	IMLR
<59.8/0.05	$4.5^{+2.2}_{-2.1} \times 10^{-4}$	$1.1^{+0.2}_{-0.1} \times 10^{-4}$	$2.6^{+0.1}_{-0.1} \times 10^{-4}$
<119.5/0.10	$2.4^{+0.7}_{-0.7} \times 10^{-3}$	$3.4^{+0.5}_{-0.5} \times 10^{-4}$	$7.4^{+0.3}_{-0.3} \times 10^{-4}$
<179.3/0.14	$4.2^{+0.9}_{-1.4} \times 10^{-3}$	$7.4^{+1.0}_{-1.0} \times 10^{-4}$	$1.4^{+0.5}_{-0.5} \times 10^{-3}$
<338.6/0.27	$1.6^{+1.0}_{-1.0} \times 10^{-2}$	$1.2^{+0.6}_{-0.5} \times 10^{-3}$	$3.0^{+0.4}_{-0.3} \times 10^{-3}$
<537.8/0.43	$3.6^{+2.4}_{-2.4} \times 10^{-2}$	$2.4^{+1.4}_{-1.3} \times 10^{-3}$	$4.6^{+0.8}_{-0.7} \times 10^{-3}$

**Fig. 7.** (a) Cumulative mass,  $M(<R)$ , within the 3-dimensional radius,  $R$ , for O, Fe, and Mg in A 262, based on the combination of the abundance determination with Suzaku and the gas mass profile with Chandra and XMM-Newton. (b) Ratio of the O, Fe, and Mg mass in units of  $M_{\odot}$  to the  $K$  band luminosity in units of  $L_{\odot}$  (OMLR, IMLR, and MMLR, respectively) against the 3-dimensional radius. The black crosses, black diamonds, and gray diamonds show the OMLR, IMLR, MMLR, respectively.**Table 7.** Comparison of IMLR, OMLR and MMLR with B-band luminosity for all systems.

	IMLR	OMLR	MMLR	$r$ (kpc/ $r_{180}$ )	$k\langle T \rangle$	Reference
Suzaku						
NGC 720 ....	$1 \times 10^{-4}$	$4 \times 10^{-4}$	–	25/0.04	$\sim 0.56$ keV	Tawara et al. (2008)
NGC 5044 ...	$2.6 \times 10^{-3}$	$6.6 \times 10^{-3}$	$1.6 \times 10^{-3}$	88/0.10	$\sim 1.0$ keV	Komiyama et al. (2008)
	$3.6 \times 10^{-3}$	$9.4 \times 10^{-3}$	$2.6 \times 10^{-3}$	260/0.30		
	$6.0 \times 10^{-4}$	–	–	327/0.38		Buote et al. (2004)
Fornax .....	$4 \times 10^{-4}$	$2 \times 10^{-3}$	–	130/0.13	$\sim 1.3$ keV	Matsushita et al. (2007b)
NGC 507 ....	$6.0 \times 10^{-4}$	$2.6 \times 10^{-3}$	$3.7 \times 10^{-4}$	120/0.11	$\sim 1.5$ keV	Sato et al. (2008b)
	$1.7 \times 10^{-3}$	$6.6 \times 10^{-3}$	$1.1 \times 10^{-3}$	260/0.24		
HCG 62 .....	$2.0 \times 10^{-3}$	$6.4 \times 10^{-3}$	$1.0 \times 10^{-3}$	120/0.11	$\sim 1.5$ keV	Tokoi et al. (2008)
	$4.6 \times 10^{-3}$	$3.8 \times 10^{-2}$	$1.5 \times 10^{-3}$	230/0.21		
A 262 .....	$3.6 \times 10^{-3}$	$1.2 \times 10^{-2}$	$1.6 \times 10^{-3}$	130/0.10	$\sim 2$ keV	This work
	$6.7 \times 10^{-3}$	$3.7 \times 10^{-2}$	$2.7 \times 10^{-3}$	340/0.27		
A 1060 .....	$5.7 \times 10^{-3}$	$4.3 \times 10^{-2}$	$2.4 \times 10^{-3}$	180/0.12	$\sim 3$ keV	Sato et al. (2007a)
	$4.0 \times 10^{-3}$	$4.3 \times 10^{-2}$	$1.6 \times 10^{-3}$	380/0.25		
AWM 7 .....	$4.8 \times 10^{-3}$	$2.6 \times 10^{-2}$	$3.4 \times 10^{-3}$	180/0.11	$\sim 3.5$ keV	Sato et al. (2008a)
	$7.6 \times 10^{-3}$	$3.1 \times 10^{-2}$	$6.7 \times 10^{-3}$	360/0.22		
XMM-Newton						
Centaurus ...	$4 \times 10^{-3}$	$3 \times 10^{-2}$	–	190/0.11	$\sim 4$ keV	Matsushita et al. (2007a)

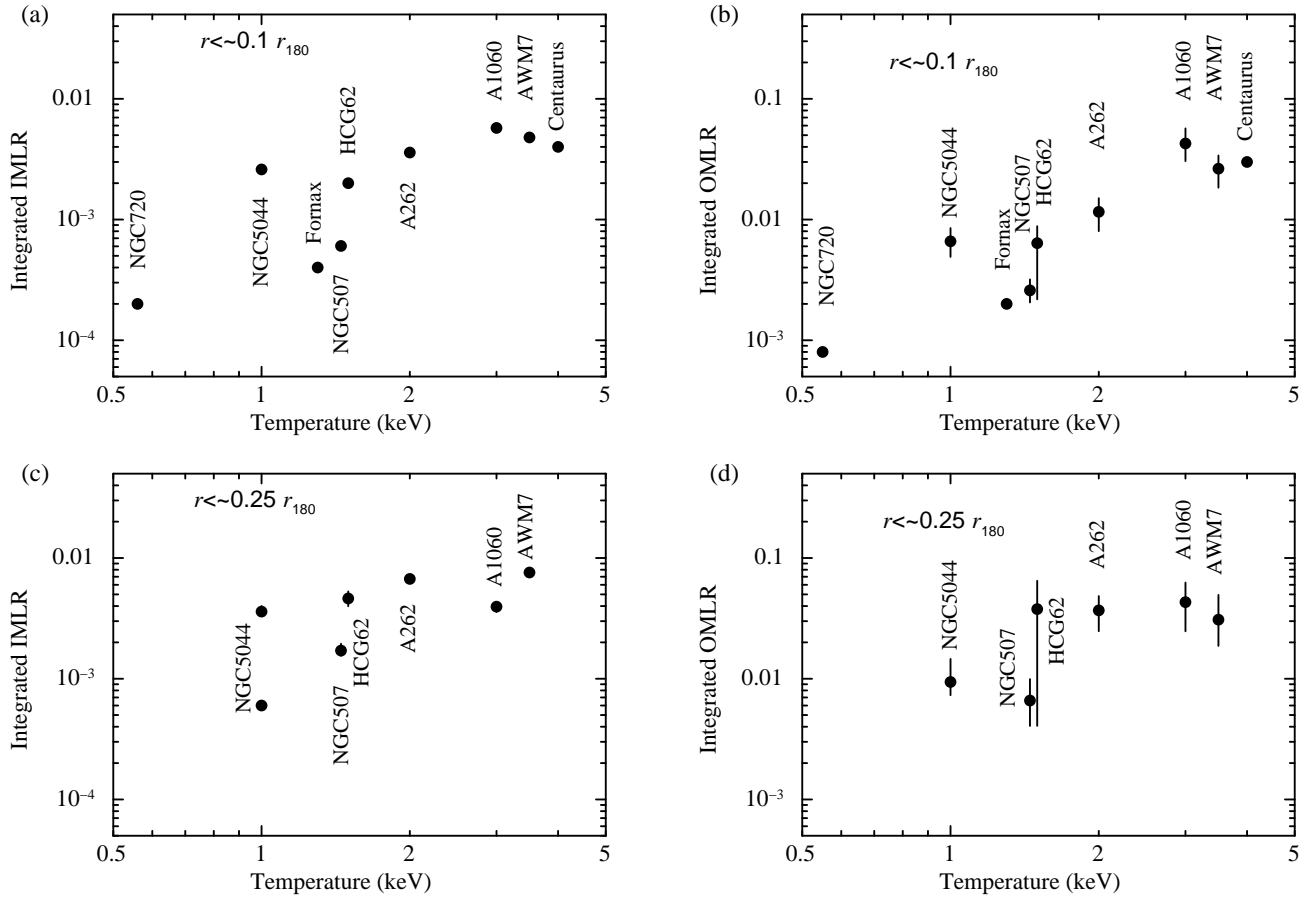


**Fig. 8.** Comparison of IMLR (a) and (c), and OMLR (b) and (d) with B-band luminosity to the other clusters and groups within  $\sim 0.1 r_{180}$  and  $\sim 0.25 r_{180}$  region, respectively.

We also derived the MLRs with B-band luminosity using an appropriate color  $B - K = 4.2$  for early-type galaxies given by Lin & Mohr (2004), along with the Galactic extinction,  $A_B = 0.267$ , from NED in the direction of A 262. The integrated values of OMLR, IMLR, and MMLR with B-band within  $r \lesssim 540$  kpc turned out to be  $\sim 7.1 \times 10^{-2}$ ,  $\sim 9.0 \times 10^{-3}$ , and  $\sim 4.7 \times 10^{-3} M_{\odot}/L_{\odot}$ , respectively. Comparing these B-band MLRs with those of other clusters and groups measured within  $\sim 0.1 r_{180}$  and  $\sim 0.25 r_{180}$ , the A 262 points fall between those of clusters and groups, in particular within  $\sim 0.1 r_{180}$ . In other radii, the A262 results are consistent with those for the poor clusters as shown in table 7 and figure 8. The tendency that smaller systems with lower gas temperature tend to exhibit smaller MLRs, as shown previously by Makishima et al. (2001) and by Sato et al. (2008b), is clearly indicated by the present addition of the A 262 data.

## 5. Summary and conclusion

Based on the Suzaku observation of A 262, we studied spatial distribution of temperature and metal abundances for O, Mg, Si, S, and Fe up to  $\sim 0.43 r_{180}$ . The ICM temperature decreases mildly from  $\sim 2.3$  keV to  $\sim 1.5$  keV

in the outer region. The abundances of Mg, Si, S, and Fe drop from subsolar levels at the center to  $\sim 1/5$  solar in the outermost region, while the O abundance shows a flatter distribution around  $\sim 0.5$  solar compared with the other metals. The abundance ratios, O/Fe, Mg/Fe, Si/Fe, and S/Fe for A 262 are similar to those of other clusters with  $kT = 3-4$  keV and groups with  $kT \sim 1.5$  keV. The number ratio of SNe II to Ia which contributed for the ICM enrichment is  $3.0 \pm 0.6$ , consistent with the values for other clusters and groups. The derived MLRs with B-band luminosity fall between the data for clusters and groups measured within a radius of  $\sim 0.1 r_{180}$ . Thus, the A 262 data gives us a good connection concerning the global picture of the metal enrichment process between clusters and groups of galaxies.

Authors are grateful to T. Ohashi for valuable comments and discussions. We also thank the referee for providing valuable comments. Part of this work was financially supported by the Ministry of Education, Culture, Sports, Science and Technology of Japan, Grant-in-Aid for Scientific Research Nos. 18740011, 19840043.

This research has made use of the NASA/IPAC Extragalactic Database (NED) which is operated by the JPL, under contract with NASA.

## References

- Anders, E., & Grevesse, N. 1989, *Geochim. Cosmochim. Acta*, 53, 197
- Arimoto, N., Matsushita, K., Ishimaru, Y., Ohashi, T., & Renzini, A. 1997, *ApJ*, 477, 128
- Arnaud, M., Rothenflug, R., Boulade, O., Vigroux, L., & Vangioni-Flam, E. 1992, *A&A*, 254, 49
- Blanton, E. L., Sarazin, C. L., McNamara, B. R., & Clarke, T. E. 2004, *ApJ*, 612, 817
- Böhringer, H., Matsushita, K., Finoguenov, A., Xue, Y., & Churazov, E. 2005, *Advances in Space Research*, 36, 677
- Buote, D. A. 2000, *MNRAS*, 311, 176
- Buote, D. A., Brighenti, F., & Mathews, W. G. 2004, *ApJL*, 607, L91
- David, L. P., Slyz, A., Jones, C., Forman, W., Vrtilik, S. D., & Arnaud, K. A. 1993, *ApJ*, 412, 479
- David, L. P., Jones, C., & Forman, W. 1996, *ApJ*, 473, 692
- De Grandi, S., & Molendi, S. 2001, *ApJ*, 551, 153
- de Plaa, J., Werner, N., Bleeker, J. A. M., Vink, J., Kaastra, J. S., & Méndez, M. 2007, *A&A*, 465, 345
- de Plaa, J., et al. 2006, *A&A*, 452, 397
- Dickey, J. M., & Lockman, F. J. 1990, *ARA&A*, 28, 215
- Fabian, A. C., Sanders, J. S., Taylor, G. B., Allen, S. W., Crawford, C. S., Johnstone, R. M., & Iwasawa, K. 2006, *MNRAS*, 366, 417
- Fabian, A. C., Sanders, J. S., Taylor, G. B., & Allen, S. W. 2005, *MNRAS*, 360, L20
- Fabian, A. C., Sanders, J. S., Ettori, S., Taylor, G. B., Allen, S. W., Crawford, C. S., Iwasawa, K., & Johnstone, R. M. 2001, *MNRAS*, 321, L33
- Fanti, C., Fanti, R., de Ruiter, H. R., & Parma, P. 1986, *A&AS*, 65, 145
- Finoguenov, A., David, L. P., & Ponman, T. J. 2000, *ApJ*, 544, 188
- Finoguenov, A., Arnaud, M., & David, L. P. 2001, *ApJ*, 555, 191
- Finoguenov, A., Matsushita, K., Böhringer, H., Ikebe, Y., & Arnaud, M. 2002, *A&A*, 381, 21
- Fujimoto, R., et al. 2007, *PASJ*, 59, 133
- Fukazawa, Y., Makishima, K., Tamura, T., Ezawa, H., Xu, H., Ikebe, Y., Kikuchi, K., & Ohashi, T. 1998, *PASJ*, 50, 187
- Fukazawa, Y., Makishima, K., Tamura, T., Nakazawa, K., Ezawa, H., Ikebe, Y., Kikuchi, K., & Ohashi, T. 2000, *MNRAS*, 313, 21
- Fukazawa, Y., Makishima, K., & Ohashi, T. 2004, *PASJ*, 56, 965
- Gastaldello, F., & Molendi, S. 2002, *ApJ*, 572, 160
- Gastaldello, F., Buote, D. A., Humphrey, P. J., Zappacosta, L., Bullock, J. S., Brighenti, F., & Mathews, W. G. 2007, *ApJ*, 669, 158
- Gastaldello, F., et al. in preparation
- Humphrey, P. J., & Buote, D. A. 2006, *ApJ*, 639, 136
- Ishisaki, Y., et al. 2007, *PASJ*, 59, 113
- Iwamoto, K., Brachwitz, F., Nomoto, K., Kishimoto, N., Umeda, H., Hix, W. R., & Thielemann, F.-K. 1999, *ApJS*, 125, 439
- Komiyama, M., et al. 2008, in preparation
- Koyama, K., et al. 2007, *PASJ*, 59, 23
- Kushino, A., Ishisaki, Y., Morita, U., Yamasaki, N. Y., Ishida, M., Ohashi, T., & Ueda, Y. 2002, *PASJ*, 54, 327
- Lin, Y.-T., & Mohr, J. J. 2004, *ApJ*, 617, 879
- Lodders, K. 2003, *ApJ*, 591, 1220
- Lumb, D. H., Warwick, R. S., Page, M., & De Luca, A. 2002, *A&A*, 389, 93
- Makishima, K., et al. 2001, *PASJ*, 53, 401
- Markevitch, M., et al. 1998, *ApJ*, 503, 77
- Matsushita, K., Ohashi, T., & Makishima, K. 2000, *PASJ*, 52, 685
- Matsushita, K., Finoguenov, A., Böhringer, H. 2003, *A&A*, 401, 443
- Matsushita, K., Böhringer, H., Takahashi, I., & Ikebe, Y. 2007b, *A&A*, 462, 953
- Matsushita, K., et al. 2007a, *PASJ*, 59, 327
- McCammon, D., et al. 2002, *ApJ*, 576, 188
- Neill, J. D., Brodie, J. P., Craig, W. W., Hailey, C. J., & Misch, A. A. 2001, *ApJ*, 548, 550
- Nomoto, K., Tominaga, N., Umeda, H., Kobayashi, C., & Maeda, K. 2006, *Nuclear Physics A*, 777, 424
- O'Sullivan, E., Vrtilik, J. M., Kempner, J. C., David, L. P., & Houck, J. C. 2005, *MNRAS*, 357, 1134
- Parma, P., de Ruiter, H. R., Fanti, C., & Fanti, R. 1986, *A&AS*, 64, 135
- Peres, C. B., Fabian, A. C., Edge, A. C., Allen, S. W., Johnstone, R. M., & White, D. A. 1998, *MNRAS*, 298, 416
- Peterson, J. R., Kahn, S. M., Paerels, F. B. S., Kaastra, J. S., Tamura, T., Bleeker, J. A. M., Ferrigno, C., & Jernigan, J. G. 2003, *ApJ*, 590, 207
- Rasmussen, J., & Ponman, T. J. 2007, *MNRAS*, 380, 1554
- Renzini, A., Ciotti, L., D'Ercole, A., & Pellegrini, S. 1993, *ApJ*, 419, 52
- Renzini, A. 1997, *ApJ*, 488, 35
- Sanders, J. S., & Fabian, A. C. 2002, *MNRAS*, 331, 273
- Sanders, J. S., & Fabian, A. C. 2006, *MNRAS*, 371, 1483
- Sanders, J. S., & Fabian, A. C. 2007, *MNRAS*, 381, 1381
- Simionescu, A., Werner, N., Finoguenov, A., Böhringer, H., & Brüggén, M. 2008, *A&A*, 482, 97
- Sato, K., et al. 2007a, *PASJ*, 59, 299
- Sato, K., Tokoi, K., Matsushita, K., Ishisaki, Y., Yamasaki, N. Y., Ishida, M., & Ohashi, T. 2007, *ApJL*, 667, L41
- Sato, K., Matsushita, K., Ishisaki, Y., Yamasaki, N. Y., Ishida, M., Sasaki, S., & Ohashi, T. 2008, *PASJ*, 60, S333
- Sato, K., Matsushita, K., Ishisaki, Y., Yamasaki, N. Y., Ishida, M., & Ohashi, T. 2008, *PASJ*, in press
- Tamura, T., Kaastra, J. S., Makishima, K., & Takahashi, I. 2003, *A&A*, 399, 497
- Tamura, T., Kaastra, J. S., den Herder, J. W. A., Bleeker, J. A. M., & Peterson, J. R. 2004, *A&A*, 420, 135
- Tawara, Y., et al. 2008, *PASJ*, 60, S307
- Tokoi, K., et al. 2008, *PASJ*, 60, S317
- Vikhlinin, A., Kravtsov, A., Forman, W., Jones, C., Markevitch, M., Murray, S. S., & Van Speybroeck, L. 2006, *ApJ*, 640, 691
- Werner, N., de Plaa, J., Kaastra, J. S., Vink, J., Bleeker, J. A. M., Tamura, T., Peterson, J. R., & Verbunt, F. 2006a, *A&A*, 449, 475
- White, D. A. 2000, *MNRAS*, 312, 663
- Xu, H., et al. 2002, *ApJ*, 579, 600